Pergamon

Int. J. Heat Mass Transfer. Vol. 37, No. 17, pp. 2715–2722, 1994

0017–9310/94 $7.00 + 0.00

0017–9310(94)E0094–B

Numerical modeling of the steady-state two-phase closed thermosyphon

Z. J. ZUO and F. S. GUNNERSON†

University of Central Florida, College of Engineering, Two-phase Flow and Heat Transfer Laboratories, Orlando, FL 32816, U.S.A.

(*Received* 23 *June* 1993 *and in final form* 28 *February* 1994)

Abstract—The steady-state performance of the gravity-assisted, two-phase, closed thermosyphon was modeled from first principles. Liquid-film momentum advection and axial normal stress, typically neglected by previous investigators, were included and shown to be important to the thermosyphon performance. The model presented also expanded previous analyses to include both temperature and heat-flux controlled thermosyphons and thermosyphons with mixed or other external boundary conditions. Numerical techniques were incorporated to solve the nonlinear governing equations and respective boundary conditions. A series of thermosyphon experiments were conducted. Predictions from the model agree well with experimental results. The parametric effects of operating temperatures, geometry, working fluid inventory and condenser thermal capacity were studied. The model presented could be used for optimization studies and design of thermosyphons.

1. INTRODUCTION

FIGURE 1 illustrates a simple, gravity-assisted, closed thermosyphon. By incorporating the thermally efficient evaporation and condensation processes, the device is capable of transporting exceedingly high rates of thermal energy. In contrast to a heat pipe which utilizes capillary forces to return the condensate to the evaporator, the thermosyphon relies upon gravitational or centrifugal forces for liquid return. During operation, heat is transferred to the working fluid inside the thermosyphon through the evaporator region, and the working fluid is turned to vapor. The vapor rises through the adiabatic region to the condenser, where it condenses and liberates the latent heat. The condensate is returned to the evaporator as a liquid film by gravity.

Due to their simple construction, small thermal resistance, broad operating limits and low fabrication cost, thermosyphons have found a spectrum of applications. Examples include HVAC dehumidification, solar heating systems, preservation of permafrost, deicing of road-ways, thermal energy storage systems, liquid-oxygen storage systems, turbine blade and microelectronic circuit cooling [1, 2].

The heat transfer characteristics of a thermosyphon are limited by a host of thermophysical constraints including the thermodynamics of the working fluid, evaporator dry-out or critical heat flux (CHF), entrainment of return condensate (flooding limit) and the effectiveness of the condensation process.

The performance of the thermosyphon has been extensively studied in recent years. The first comprehensive analysis of the two-phase, closed thermosyphon was made by Lee and Mital [3]. They experimentally studied the effects of various controlling variables (amount of working fluid, condenser to evaporator length ratio, operating temperatures

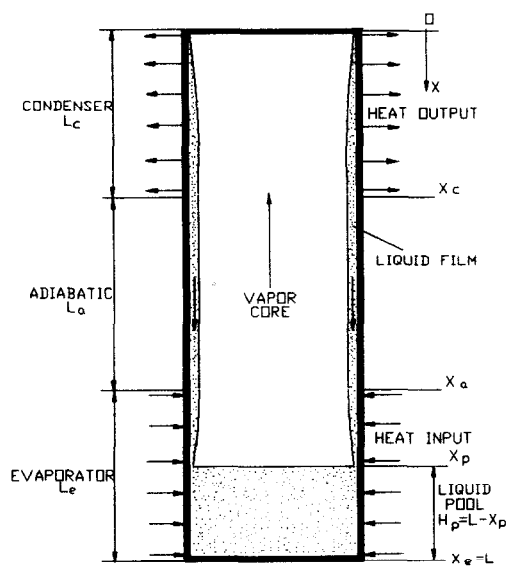

FIG. 1. A simple gravity-assisted two-phase closed thermosyphon.

† Author to whom correspondence should be addressed.

NOMENCLATURE

Bo	Bond number, $(4\rho_l g R^2/\sigma)^{1/2}$
C_f	friction coefficient
C_p	liquid specific heat
dx	grid size [m]
g	gravitational acceleration [m s^{-2}]
h	heat transfer coefficient [W m^{-2} K^{-1}]
h_{fg}	latent heat of vaporization [kJ kg^{-1}]
H_p	depth of the liquid pool [m]
k_l	liquid thermal conductivity [W m^{-1} K^{-1}]
L	length of the thermosyphon [m]
M	total amount of working fluid inside the thermosyphon [kg]
$\dot{m}_c$	mass flow rate of condenser cooling water [kg s^{-1}]
P	pressure [Pa]
Pr	liquid Prandtl number, $\mu_l C_p/k_l$
$\dot{q}''$	wall heat flux [W m^{-2}]
R	inner radius of the thermosyphon [m]
r	vapor core radius [m]
Re	Reynolds number, $4\Gamma/\mu$
T	temperature [K]
u	velocity [m s^{-1}]
V	vapor condensation velocity [m s^{-1}]
x	axial distance from the top end of thermosyphon [m].

Greek symbols

Γ	liquid mass flow rate per unit tube perimeter [kg s^{-1} m^{-1}]
δ	liquid film thickness [m]
μ	dynamic viscosity [N s m^{-2}]
ν	kinematic viscosity [m^2 s^{-1}]
ρ	density [kg m^{-3}]
σ	liquid surface tension [N m^{-1}]
τ	shear stress [N m^{-2}]
φ	phase change correction factor.

Subscripts

a	adiabatic region
atm	atmospheric
c	condenser region
e	evaporator region
i	phase interface
in	inlet condenser cooling water
l	liquid phase
p	liquid pool surface
s	saturation
w	tube wall
v	vapor phase.

and pressures) on the thermosyphon performance. Shiraishi *et al.* [4] experimentally studied the heat transfer processes in both the evaporator and condenser regions and proposed empirical heat transfer coefficients. Tien and Chung [5] developed a semi-empirical relationship for determining the flooding limit. A thermosyphon CHF correlation was developed by Imura *et al.* [6]. Because of the inherent complexities in modeling the physical processes and the difficulties in solving the nonlinear governing equations, most previous analytical studies focused on isolated phenomena, such as the heat transfer in the liquid pool or liquid film and the mechanisms of flooding.

Dobran [7] first provided a comprehensive model for two-phase, closed thermosyphons. Reed and Tien [8] further developed the model to include thermosyphon transient behaviors and successfully analyzed the operating limits for dry-out and flooding. Previous studies, however, assumed that changes in the liquid and vapor flow rates in the axial direction ($d\Gamma/dx$) are constant for each region; an assumption which might not be true for thermosyphons exposed to constant temperature instead of constant heat flux heat sources or sinks. Liquid-film momentum advection and normal viscous stress were usually neglected, which with the previous assumption can introduce errors in predicting thermosyphon behavior. In practice, most thermosyphon applications incorporate nearly isothermal or forced-convective condenser cooling instead of constant heat flux. Sometimes the thermosyphon evaporator region may be exposed to discrete heat sources (like in the microelectronic circuit cooling). For these cases, the assumptions and omissions made in previous models might cause even more significant errors. No analytical studies have been found dealing with effects of the working fluid inventory, effective-mass flow rate of the condenser cooling water, and the evaporator to condenser length ratio L_e/L_c; each of which is extremely important to the performance, stability and operating limits of the thermosyphon.

As illustrated in Fig. 1, modeling of a two-phase closed thermosyphon requires a fundamental understanding of the following interrelated physical processes: (1) heat addition through the evaporator wall; (2) boiling in the evaporator region (both liquid pool and liquid film); (3) condensation in the condenser region; (4) heat conduction through the condenser wall; and (5) movement of the vapor core and the liquid film. Compared with the wicked heat pipe, thermosyphon transients occur much faster, in part because of the thermal response delay to heat transfer introduced by the wetted wick [9]. Steady-state performance of the thermosyphon is the focus of this work.

The study presented here is an addition and exten-

sion to previous works to model the behavior of the gravity-assisted thermosyphon. A comprehensive system model is developed from the basic conservation laws, and numerical techniques are incorporated to solve the nonlinear governing equations. The thermophysical effects of liquid-film momentum advection and normal stress, which have not been considered in previous studies, are included herein. The model is applicable for temperature or heat-flux controlled thermosyphons and thermosyphons with mixed or other external boundary conditions. From the model, most operating parameters such as the vapor temperature, the liquid-film thickness and the mass fluxes, as well as the operating limits (dry-out and flooding) associated with the steady-state performance, can be predicted. In addition, the parametric effects of operating temperature, geometry, working fluid inventory and condenser cooling water mass flow rate were studied. Within this paper, the predictions were compared with the experimental data and other investigators' results.

2. NUMERICAL MODEL

Steady-state behavior of the simple thermosyphon is typically modeled using the following assumptions: (1) the vapor and liquid are one-dimensional, steady-state Newtonian flows; (2) compressibility of the vapor is negligible; (3) the vapor and the liquid are both at saturation temperature; (4) pressure drop in the liquid film is negligible; and (5) the axial conduction and the viscous dissipation are negligible. These assumptions are common to most two-phase annular flow studies [2] and have been supported by experimental observations [8, 10].

For the falling liquid film, the continuity and momentum equations are:

$$\frac{\mathrm{d}[(R^2-r^2)u_\mathrm{l}]}{\mathrm{d}x} = 2RV \tag{1}$$

$$\rho_\mathrm{l}\frac{\mathrm{d}}{\mathrm{d}x}[(R^2-r^2)u_\mathrm{l}^2]-\frac{\mathrm{d}}{\mathrm{d}x}\left[(R^2-r^2)\tfrac{4}{3}\mu_\mathrm{l}\frac{\mathrm{d}u_\mathrm{l}}{\mathrm{d}x}\right] - (R^2-r^2)\rho_\mathrm{l}g+2R\tau_\mathrm{w}+2r\tau_\mathrm{i}=0. \tag{2}$$

In equation (2), the first term corresponds to the total momentum change (including momentum advection) and the second term accounts for axial normal stress in the liquid film. The final three terms correspond to gravity, wall shear stress and interfacial shear stress, respectively. Unlike previous studies, the momentum advection contribution and the normal stress term are included. Both of these terms affect thermosyphon performance. The normal stress term is also important in the numerical solution procedure.

The wall shear stress and the interfacial shear stress are modeled as:

$$\tau_\mathrm{w} = \tfrac{1}{2}\rho_\mathrm{l}u_\mathrm{l}^2C_\mathrm{fw} \quad \tau_i = \tfrac{1}{2}\rho_\mathrm{v}(u_\mathrm{v}+u_\mathrm{l})^2C_\mathrm{fi} \tag{3}$$

where u_v and u_l are both positive in magnitude but opposite in direction.

Friction coefficients C_fw and C_fi common to the literature [8, 11–14] include:

$$C_\mathrm{fw} = \frac{16}{Re_\mathrm{l}} \quad \text{(Laminar liquid film, } Re_\mathrm{l} \leqslant 2040) \tag{4}$$

$$C_\mathrm{fw} = 0.079Re_\mathrm{l}^{-1/4} \quad \text{(Turbulent liquid film, } Re_\mathrm{l} > 2040) \tag{5}$$

$$C_\mathrm{fi} = \frac{16}{Re_\mathrm{v}}\frac{\varphi}{\mathrm{e}^\varphi-1} \quad \text{(Laminar vapor core, } Re_\mathrm{v} \leqslant 2040) \tag{6}$$

where φ is a correction factor accounting for the effects of phase change: $\varphi = -\rho_\mathrm{l}VR/(4\mu_\mathrm{v})$

$$C_\mathrm{fi} = \frac{Re_\mathrm{v}^{0.33}}{1525} \quad \text{(Transition region, } 2040 < Re_\mathrm{v} < 4000) \tag{7}$$

$$C_\mathrm{fi} = 0.005+x_1(\delta/R)^{x_2} \quad \text{(Turbulent vapor core, } Re_\mathrm{v} \geqslant 4000) \tag{8}$$

where $x_1 = 0.2574(Bo/2)^{x_2}10^{9.07/Bo}$ and $x_2 = 1.63+4.74/Bo$.

Considering that the conduction and convection heat transfer at the liquid–vapor interface inside the thermosyphon are much smaller than the transport of latent heat from phase change, the energy equation for liquid film flow is:

$$V = \frac{\dot{q}''}{h_\mathrm{fg}\rho_\mathrm{l}} = \frac{h(T_\mathrm{s}-T_\mathrm{w})}{h_\mathrm{fg}\rho_\mathrm{l}} \tag{9}$$

where the film heat transfer coefficient h is defined as [8]:

$$h = \frac{k_\mathrm{l}}{\delta} \quad \text{(Laminar liquid film, } Re_\mathrm{l} \leqslant 2040) \tag{10}$$

$$h = \frac{0.056Re_\mathrm{l}^{-1/5}\,Pr^{1/3}\,k_\mathrm{l}}{(\nu_\mathrm{l}^2/g)^{1/3}} \quad \text{(Turbulent liquid film, } Re_\mathrm{l} > 2040). \tag{11}$$

For the upward vapor core flow, the continuity equation can be written as:

$$\rho_\mathrm{v}\frac{\mathrm{d}(r^2u_\mathrm{v})}{\mathrm{d}x} = \rho_\mathrm{l}2RV. \tag{12}$$

Combining equation (12) with the liquid-film continuity equation (1) yields:

$$\rho_\mathrm{l}\frac{\mathrm{d}[(R^2-r^2)u_\mathrm{l}]}{\mathrm{d}x} = \rho_\mathrm{v}\frac{\mathrm{d}(r^2u_\mathrm{v})}{\mathrm{d}x} \tag{13}$$

or in integrated form:

$$\rho_\mathrm{l}(R^2-r^2)u_\mathrm{l} = \rho_\mathrm{v}r^2u_\mathrm{v}. \tag{14}$$

During steady-state operation, the relationship in

equation (14) implies that the downward mass flow rate of liquid film equals the upward mass flow rate of vapor core at any cross section of the thermosyphon. From the liquid-film model (equations (1), (2) and (9)), the vapor core velocity can be evaluated:

$$u_v = \frac{\rho_l}{\rho_v}\frac{R^2 - r^2}{r^2}u_l. \quad (15)$$

Due to the assumptions made, it is not necessary to include momentum and energy equations for the vapor core.

For the liquid pool, the continuity and energy equations are:

$$\rho_l(R^2 - r_p^2)u_{lp} = \rho_v r_p^2 u_{vp} \quad (16)$$

$$\dot{q}_e'' 2RH_p = \rho_v r_p^2 u_{vp} h_{fg}. \quad (17)$$

Equations (16) and (17) imply that mass and energy flowing into the liquid pool are equal to those flowing out of the liquid pool.

The boundary conditions for u_l and r are as follows:

(i) at the top end of the thermosyphon ($x = 0$),

$$u_l = 0 \quad r = R \quad (18)$$

(ii) at the liquid pool surface ($x = x_p$), from equations (16) and (17):

$$\rho_l[R^2 - r_p^2]u_{lp} = \frac{\dot{q}_e'' 2RH_p}{h_{fg}}. \quad (19)$$

In addition to these basic governing equations and boundary conditions, relations for the overall conservation of mass and energy in the entire thermosyphon system are also needed for calculating the liquid-pool depth and determining the saturated vapor temperature. These respective equations are:

$$M = \pi R^2 H_p \rho_l + \int_0^{x_p} [\pi r^2 \rho_v + \pi(R^2 - r^2)\rho_l]\,dx \quad (20)$$

$$\int_0^{x_c} h(T_s - T_{wc})\,dx = \int_{x_a}^{x_e} h(T_{we} - T_s)\,dx \quad (21)$$

where the heat transfer coefficient h in the liquid pool is modeled as [4]:

$$h = 0.32\frac{\rho_l^{0.65} k_l^{0.3} C_p^{0.7} g^{0.2}}{\rho_v^{0.25} h_{fg}^{0.4} \mu_l^{0.1}}\left(\frac{P}{P_{atm}}\right)^{0.23} \dot{q}_e''^{0.4}. \quad (22)$$

3. SOLUTION METHOD

Considering that the liquid-film thickness is very small compared with the pipe radius, it is reasonable to assume that $(\delta/R)^2$ is negligible relative to unity. This simplifying assumption assists in the solution to the model.

The continuity, momentum and energy equations for the liquid-film flow were solved using finite-difference methods. Because of the nonlinearity of the governing equations and boundary conditions, care must be taken when solving equations (1), (2) and (9) [15]. Generally, convergence and uniqueness of solutions of a numerical method depend upon the initial guesses and the grid size. The grid size also affects the solution accuracy. In the present work, the results from Nusselt's theory [16] were used as the first initial guesses. The liquid-film model was solved without the interfacial shear stress term, and the results then used as the second guess. A numerical technique called 'numerical switch' was then used for further solutions. With 10% of the interfacial shear stress considered in the liquid-film momentum equation, the model was solved with the results used as the initial values for next solution step. Then 20% of the interfacial shear stress was considered and the same procedure was repeated until all the interfacial shear stress has been included. The relaxation technique [17] was also used to prevent numerical over-oscillation or divergence.

Operating parameters such as the liquid-film thickness, mass fluxes, liquid-pool depth and saturated vapor temperature can be calculated directly from the model. In addition, the operating limits such as dry-out and flooding can also be predicted.

In steady state, pool dry-out and film dry-out are essentially the same [8]. Once the depth of liquid pool becomes zero, a liquid-limited dry-out condition has been reached. The zero-depth liquid pool also corresponds to the minimum quantity of working fluid required for stable performance under specified conditions.

Physically, flooding implies that the local shear stresses on the liquid film become larger than the gravitational force. This resultant net upward force retards the downward liquid-film flow and results in an unstable flow pattern. In the present solution scheme, changes in the liquid-film thickness with respect to the heat input are checked at each location, and an unbounded rate of change indicates that flooding occurs [8].

The model presented can be used to evaluate parametrically heat transfer performance of the thermosyphon. The optimum working fluid inventory, for example, is herein predicted and compared with experimental results. The optimum evaporator to condenser length ratio (L_e/L_c) for the thermosyphon used in the experiments is also discussed.

The minimum working fluid (water) inventories at various heat transfer rates are numerically calculated using different grid sizes. As expected, the solution accuracy of a larger grid size (such as $dx = 0.1$ m) is not as good as that of a smaller grid size; however, the trend is still predicted well. Once the grid size is small ($dx < 0.02$ m), the solution accuracy becomes less sensitive to the grid size. This indicates that, for rough calculations, using a large grid size can greatly reduce the computer time. The results from a large-grid-size calculation could also be used as the initial value estimates for more precise calculations. For the numerical results presented herein, a grid size of $dx = 0.01$ m was chosen.

4. EXPERIMENTAL STUDY

A series of thermosyphon experiments have been conducted within the Two-phase Flow and Heat Transfer Laboratories at the University of Central Florida.

The thermosyphon used in the test series was made from a 19 mm (3/4 in.) standard copper tube, with a 381 mm (15 in.) long immersed evaporator region, a 610 mm (24 in.) long adiabatic region, and an 812 mm (32 in.) long condenser region, giving an overall length of 1803 mm (71 in.). During operation, the evaporator region was immersed in a constant-temperature hot-water bath, and the condenser region was surrounded by a water cooling jacket to remove the heat. The working fluid used in the experiments was distilled water.

Fifteen Type-J thermocouples were used to monitor the temperatures at different locations. A 21X Micrologger was used to continually monitor and record the thermal behavior during experiments. Gage pressure inside the thermosyphon was also measured during operation.

One purpose of these esperiments was to assess the optimum quantity of working fluid to yield the maximum heat transfer ability under specified operating conditions.

5. COMPARISONS AND DISCUSSIONS OF RESULTS

The model presented has been solved for different operating conditions. The results were compared with experimental and other investigators' results.

Figure 2 compares the analytical and experimental heat transfer rates at various working fluid (water) inventories. The operating conditions are: $T_e = 65°C$, $T_{in} = 22°C$, and $\dot{m}_c = 0.0176$ kg s^{-1}. As shown, the agreement between prediction and experiment is good. In Fig. 2, point A indicates the minimum working fluid inventory required for stable performance, and corresponds to a zero depth of the liquid pool within the evaporator. As more working fluid is added into the thermosyphon, a liquid pool is formed. The boiling heat transfer mechanism in the liquid pool is complicated, and an empirical heat transfer coefficient (equation 22)) from Shiraishi *et al.* [4] was used in the model. Physically, increasing hydrostatic pressure in the liquid pool by increasing pool depth will enhance the heat transfer, but will also cause higher saturation temperatures. This effect is important especially at low operating vacuum pressures [4]. Point B indicates the highest heat transfer rate and correspondingly the optimum working fluid inventory. As the quantity of working fluid further increases, the effect of increased saturation temperature will dominate, and the heat transfer rate will decrease slightly. The trend illustrated in Fig. 2, with an optimum working fluid inventory, has likewise been reported by previous investigators [3, 18].

Figure 3 shows the vapor core temperature at various evaporator wall temperatures while holding other parameters constant. The agreement between the predictions and the experiments is again good. Results from Nusselt theory [16] are also illustrated. As expected, as the evaporator wall temperature (driving force for heat transfer) increases, the interfacial shear stress between the vapor core and the liquid film becomes important, which makes Nusselt's results deviate further from the experimental data.

Figure 4 shows the effect of mass flow rate of the condenser cooling water on the thermosyphon heat transfer ability. At low condenser cooling water flow rates (<0.015 kg s^{-1}), the heat transfer ability is most sensitive to the mass flow rate of the cooling water. At higher mass flow rates, the heat transfer sensitivity becomes less. In practical applications, a minimum condenser capacity is necessary for high heat transfer rates. As expected, higher evaporator wall temperatures will increase the heat transfer rates.

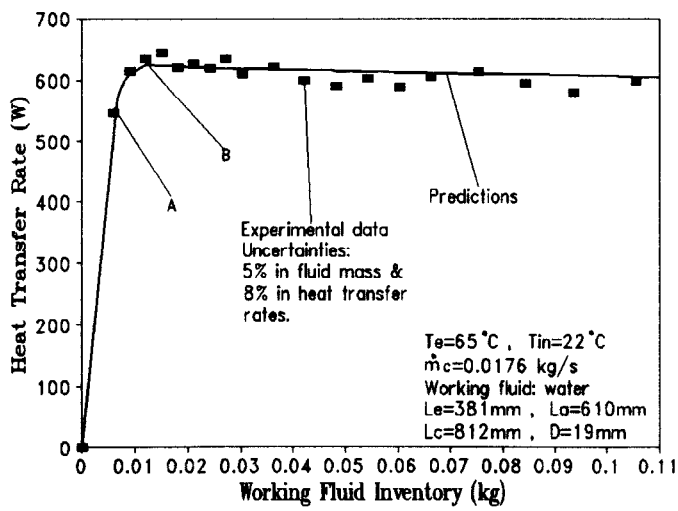

FIG. 2. Heat transfer rate vs working fluid inventory.

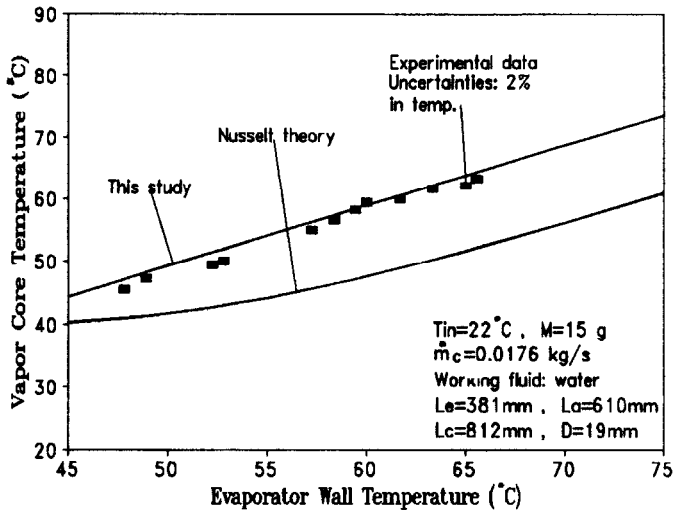

FIG. 3. Vapor core temperature vs evaporator wall temperature.

Figure 5 shows a comparison of the flooding limit predicted by the present model with those by previous models from Tien and Chung [5], Reed and Tien [8], as well as Prenger's experimental data [8]. The figure plots the liquid-film Reynolds number in the adiabatic region at the onset of flooding versus the vapor core temperature (operating temperature). As shown, there is a slight difference between the results from the present model and Reed and Tien's results. This difference might be due to effects of the first and second terms in the liquid-film momentum equation (2). The momentum advection usually lowers the heat flux at the onset of flooding, and the normal stress gives an opposite contribution. At higher vapor core temperatures ($>75°C$), the decrease in liquid viscosity contributes to higher flooding limits.

Figure 6 shows the heat transfer rate of the thermosyphon used in the present experiments for various evaporator to condenser length ratios (L_e/L_c), while the total length of the thermosyphon is kept constant (71 in.). As shown, there exists a value of L_e/L_c corresponding to the maximum heat transfer ability. This optimum value of L_e/L_c is around 0.1, which corresponds to the best distribution of evaporator (heat absorbing) and condenser (heat removing) surface areas. The optimum value of L_e/L_c is not sensitive to the evaporator wall temperature. The trend illustrated in Fig. 6 was likewise reported by Lee and Mital [3].

6. CONCLUSIONS

In the present work, the steady-state, two-phase, closed thermosyphon was successfully modeled from first principles. Numerical techniques were incorporated to solve the nonlinear governing equations. Several operating parameters and operating limits associated with steady-state performance have been predicted, and comparisons with experiments and other investigators' results show good agreement. Several important parameters (such as the working fluid

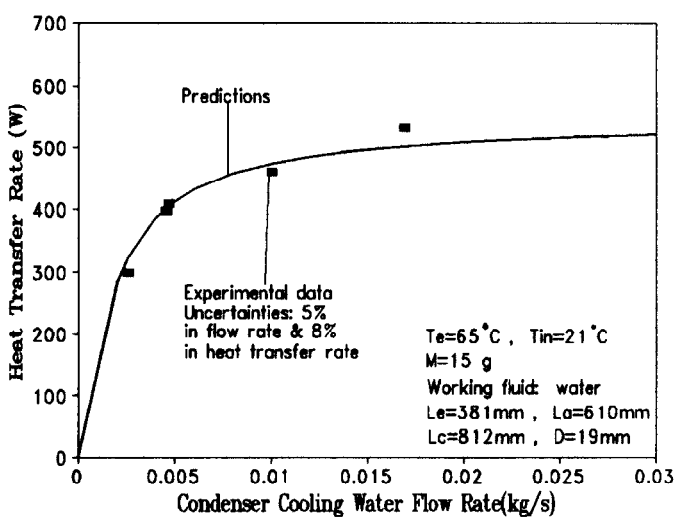

FIG. 4. Heat transfer rate vs mass flow rate of the condenser cooling water.

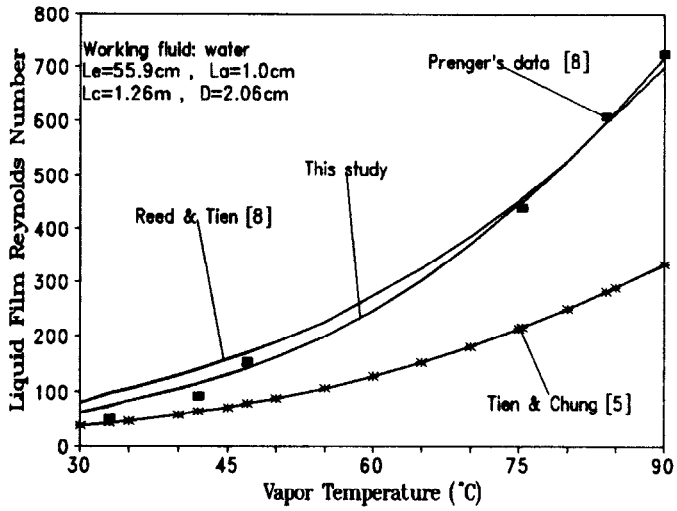

FIG. 5. Liquid-film Reynolds number at the flooding onset vs vapor core temperature.

inventory, the evaporator to condenser length ratio, etc.) have been optimized to yield the maximum heat transfer ability.

The following conclusions are drawn.

(1) Momentum advection of the liquid film lowers the heat input necessary for flooding (Fig. 5).
(2) Normal stress in the liquid film gives an opposite effect and is also important to the numerical solution procedure.
(3) There exists an optimum working fluid inventory for a temperature-controlled thermosyphon which yields the maximum heat transfer capacity (Fig. 2). The effect of working fluid inventory on the heat transfer rate is related to the heat transfer mechanism in the liquid pool. This optimum quantity depends upon the thermophysical nature of the working fluid, the operating conditions (temperature or input heat flux), geometry of the thermosyphon, and the heat transfer mechanism in the working fluid pool.
(4) The interfacial shear stress increases in importance as the heat transfer rate increases (Fig. 3).
(5) Changes of the mass flow rate of condenser cooling water significantly affect the heat transfer capacity, especially while the mass flow rate is low (Fig. 4).
(6) There is an optimum value of L_e/L_c (which corresponds to the best distribution of heat absorbing and removing areas) for the maximum heat transfer ability for the temperature-controlled thermosyphon (Fig. 6).

Experimental and analytical studies continue to evaluate the performance of thermosyphons at large heat inputs, on the micro-thermosyphon scale, and the effect of inclination angle.

Acknowledgements—Partial support of this work by NASA-KSC is gratefully acknowledged and the authors thank the many participating students for their laboratory support.

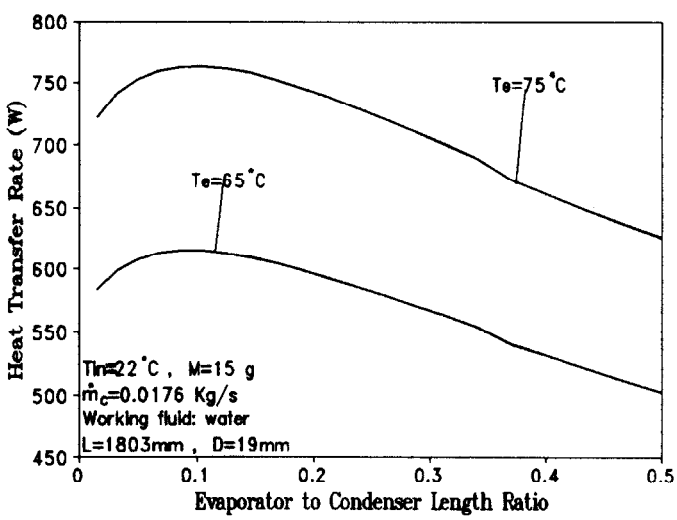

FIG. 6. Heat transfer rate vs evaporator to condenser length ratio.

REFERENCES

1. F. Dobran, Heat pipe research and development in the Americas, *Heat Recovery Systems CHP* **9,** 67–100 (1989).
2. G. S. H. Lock, *The Tubular Thermosyphon*, Chaps. 1 and 3. Oxford University Press, Oxford (1992).
3. Y. Lee and U. Mital, A two-phase closed thermosyphon. *Int. J. Heat Mass Transfer* **15,** 1695–1707 (1972).
4. M. Shiraishi, K. Kikuchi and T. Yamanishi, Investigation of heat transfer characteristics of a two-phase closed thermosyphon. In *Advances in Heat Pipe Technology* (Edited by D. A. Reay), pp. 95–104. Pergamon Press, New York (1981).
5. C. L. Tien and K. S. Chung, Entrainment limits in heat pipes, *AIAA Jl* **17,** 643–646 (1981).
6. H. Imura, K. Sasaguchi, H. Kozzai and S. Numata, Critical heat flux in a closed two-phase thermosyphon, *Int. J. Heat Mass Transfer* **26,** 1181–1188 (1983).
7. F. Dobran, Steady-state characteristics and stability thresholds of a closed two-phase thermosyphon, *Int. J. Heat Mass Transfer* **28,** 949–957 (1985).
8. J. G. Reed and C. L. Tien, Modeling of the two-phase closed thermosyphon, *ASME J. Heat Transfer* **109,** 722–730 (1987).
9. W. J. Bowman, Numerical modeling of heat-pipe transients, *J. Thermophysics* **5,** 374–379 (1991).
10. C. Casaros and F. Dobran, Experimental investigation and analytical modeling of a closed two-phase thermosyphon with imposed convection boundary conditions, *Int. J. Heat Mass Transfer* **31,** 1815–1833 (1988).
11. G. B. Wallis, *One Dimensional Two-Phase Flow*, Chap. 11. McGraw-Hill, New York (1969).
12. J. G. Collier, *Convective Boiling and Condensation*, Chap. 10. McGraw-Hill, New York (1981).
13. G. F. Hewitt, *Annular Two-Phase Flow*, Chaps. 1 and 3. Pergamon Press, New York (1970).
14. F. Blangetti and M. Naushahi, Influence of mass transfer on the momentum transfer in condensation and evaporation phenomena, *Int. J. Heat Mass Transfer* **23,** 1694–1695 (1980).
15. P. G. Huang, B. E. Launder and M. A. Leschziner, Discretization of nonlinear convection processes: a broad-range comparison of four schemes, *Computer Meth. Appl. Mech. Engng* **48,** 1–24 (1985).
16. F. P. Incropera and D. P. Dewitt, *Fundamentals of Heat and Mass Transfer*, Chap. 10. John Wiley and Sons, New York (1990).
17. D. A. Anderson, J. C. Tannehill and R. H. Pletcher, *Computational Fluid Mechanics and Heat Transfer*, Chap. 4. McGraw-Hill, New York (1984).
18. K. Negish *et al.*, Heat transfer performance of a corrugated-tube thermosyphon, *Heat Transfer (Jpn)* **20,** 144–168 (1991).